Chemical Geology 490 (2018) 13–21

Contents lists available at ScienceDirect

Chemical Geology

journal homepage: www.elsevier.com/locate/chemgeo

Distribution, redox state and (bio)geochemical implications of arsenic in present day microbialites of Laguna Brava, Salar de Atacama

María Sancho-Tomás[a,*], Andréa Somogyi[b], Kadda Medjoubi[b], Antoine Bergamaschi[b], Pieter T. Visscher[c,d], Alexander E.S. Van Driessche[e], Emmanuelle Gérard[a], María E. Farias[f], Manuel Contreras[g], Pascal Philippot[a]

[a] Institut de Physique du Globe de Paris, Paris, France
[b] Synchrotron Soleil, Gif-sur-Yvette, France
[c] University of Connecticut, Groton, USA
[d] Université Bourgogne Franche-Comté, Dijon, France
[e] Université Grenoble Alpes, Université Savoie Mont Blanc, CNRS, IRD, IFSTTAR, ISTerre, F-38000 Grenoble, France
[f] LIMLA - PROIMI - CONICET, Tucumán, Argentina
[g] Centro Ecologia Aplicada, 2-2741872 Santiago, Chile

ARTICLE INFO

Keywords:
Arsenic
Biogeochemical cycles
Microbial mats
Stromatolites
Biosignature
Synchrotron-based X-ray imaging

ABSTRACT

Understanding how microorganisms adapted to the high arsenic concentration present on early Earth requires understanding of the processes involved in the arsenic biogeochemical cycle operating in living microbial mats. To this end, we investigated a living microbial mat from Laguna Brava (Salar de Atacama, Chile), a hypersaline lake with high arsenic concentration, using an array of conventional geochemical techniques, such as X-ray diffraction, SEM-EDX and Confocal Laser Scanning Microscopy (CLSM), combined with state-of-the-art high resolution scanning imaging techniques, including X-ray micro-fluorescence (μXRF) and X-ray Absorption Near Edge Structure (XANES) mapping. This experimental approach allowed us to unravel the relationship between the microbial mat activity, mineral occurrence, arsenic speciation, distribution of major and trace elements and their relationship with the mineralogy and the exopolymeric substances (EPS). We show that As was not linked to Ca or Si, and only moderately related to Fe, resulting from sorption onto an iron (oxy)hydroxide mineral. In addition, we were able to identify organic-rich globules containing significant As but no other trace metal(loid)s, and determine the co-existence of As(III) and As(V). These observations strongly support the occurrence of microbially-mediated arsenic cycling in these microbial mats.

1. Introduction

Due to widespread volcanism and geothermal activity characteristic of the Precambrian, considerably more arsenic accumulated on the Earth's surface than today (Cabral and Beaudoin, 2007; Witt-Eickschen et al., 2009). This posed both a biochemical challenge and advantage. The challenge is a direct consequence of the fact that the most common arsenic oxyanions in Nature, arsenite (AsO_3^{-3}, As(III)) and arsenate (AsO_4^{-3}, As(V)), have a high affinity to sulfhydryl groups in amino acids, by which they can disrupt the protein function (Oremland and Stolz, 2003). Moreover, arsenate is a phosphate analogue that can displace phosphate ions in enzymatic reactions and therefore, may interfere with the cellular metabolisms (Oremland and Stolz, 2003) or lead to mutagenic effects (Lièvremont et al., 2009). To cope with these deleterious effects, microbes must have adopted strategies to detoxify arsenic, such as the arsenic resistance system (*ars* gene), which uses encoded proteins that identify and transport arsenic (Páez-Espino et al., 2009), and the less studied methylation of As species (Bentley and Chasteen, 2002). Alternatively, the arsenic redox cycling reactions could provide metabolic energy on early Earth, through bacterially-mediated As(V) reduction and, conversely, As(III) oxidation. These arsenic metabolisms can be observed today in anaerobic extant habitats, such as the hypersaline environments of the Mono Lake and Searles Lake, California (Oremland et al., 2004) and the High-Altitude Andean Lakes, such as Laguna Brava, in Salar de Atacama, and Laguna Diamante, located inside the Galan Volcano crater in Argentina (Farías

* Corresponding author.
E-mail addresses: sanchotomas@ipgp.fr (M. Sancho-Tomás), andrea.somogyi@synchrotron-soleil.fr (A. Somogyi), kadda.medjoubi@synchrotron-soleil.fr (K. Medjoubi), pieter.visscher@uconn.edu (P.T. Visscher), alexander.van-driessche@univ-grenoble-alpes.fr (A.E.S. Van Driessche), emgerard@ipgp.fr (E. Gérard), mcontreras@cea.cl (M. Contreras), philippot@ipgp.fr (P. Philippot).

https://doi.org/10.1016/j.chemgeo.2018.04.029
Received 16 December 2017; Received in revised form 23 April 2018; Accepted 25 April 2018
Available online 07 May 2018

et al., 2013; Rascovan et al., 2016).

The potential biogeochemical role of As on early Earth has been addressed in several investigations based on modern sediments and bacterial cultures. For instance, biomolecular studies have demonstrated that the arsenite oxidase enzyme *Aio* has a deeply rooted origin that predates the divergence of Archaea and Bacteria from the Last Universal Common Ancestor (Lebrun et al., 2003; Duval et al., 2008). However, very few biogeochemical data supporting this claim have been put forward so far. Recently, Sforna et al. (2014) reported the discovery of 2.7-billion-year-old microbial stromatolites from Tumbiana, in which fossilized microorganisms and biogenic minerals were associated with high concentrations of As. Based on hierarchical length-scale information of the element distribution and inter-element correlations, Sforna and colleagues argued that Tumbiana stromatolites were formed by microbial mats in an anoxic, salt-saturated lake setting, and, importantly, in which As(III) oxidation occurred either by anoxygenic photosynthesis and/or denitrification. By extension, the accumulation of As(V) in these Archaean lacustrine brines could have created niches for chemoautotrophic or heterotrophic anaerobes capable of As(V) respiration (Oremland et al., 2009).

Analogues of Precambrian ecosystems can be found today in remote areas such as the hypersaline lakes in the Altiplano andino. This environment is subject to extraordinary high UV irradiation (Cabrera and Pizarro, 1992; Albarracín et al., 2016), extreme diel temperature fluctuations typical of a desert environment, hypersaline conditions and high arsenic concentrations due to active volcanism (Lara et al., 2012). Noteworthy, in Laguna Diamante, a high-altitude Andean Lake in Argentina, sequences for arsenite oxidase and respiratory arsenate reductase have been identified in Haloarchaea. These Haloarchaea have preserved As metabolisms for a very long time, linking these to ancestral metabolisms that prevailed on ancient Earth (Rascovan et al., 2016). Haloarchaea were identified as the most abundant heterotrophic microbes in a variety of different benthic microbial ecosystems in Laguna Tebenquiche (Salar de Atacama, Chile) where As concentrations in the water column reaches 0.07 mM (Fernandez et al., 2016). In the present work, we studied microbial mats from Laguna Brava, another hypersaline lake from Salar de Atacama. This habitat may represent a potential living analogue of the ancient Earth (Farías et al., 2013). The hypersaline Laguna Brava is drained with groundwaters containing leached volcanic material (Boutt et al., 2016; Corenthal et al., 2016), in which high concentrations of arsenic and sulfide are found. Hence, the microbial metabolisms in the mats are possibly driven by anoxygenic photosynthesis using reduced sulfur and arsenic compounds (Visscher et al. in prep). Anaerobic processes could include fermentation, methanogenesis, sulfate and likely arsenate reduction. The foremost aim of the present research is to identify geochemical proxies of the As-based metabolic processes occurring within the Laguna Brava mats. To do so, we have combined X-ray diffraction, SEM-EDX and Confocal Laser Scanning Microscopy (CLSM) with synchrotron-based scanning techniques, including X-ray micro-fluorescence (μXRF), point XANES (X-ray Absorption Near Edge Structure) spectroscopy and XANES imaging (Somogyi et al., 2015).

2. Materials and methods

2.1. Site description and sampling

Field campaigns in Laguna Brava were undertaken in January 2015. Laguna Brava is one of several lakes in the southern part of the Salar de Atacama, in northern Chile (Fig. 1a), located at 2350 m above sea level. The Salar de Atacama presents a dominant halite-hosted brine nucleus surrounded by a zone where sulfate, carbonate and diatomaceous deposits occur interlayered with siliciclastic alluvium and volcanic detritus (Corenthal et al., 2016). The environment is characterized by high solar irradiation (maximum UV-AB reaches ca. 60 Wm^{-2}), large variations in the amount of brine evaporation (Boutt et al., 2016), extreme

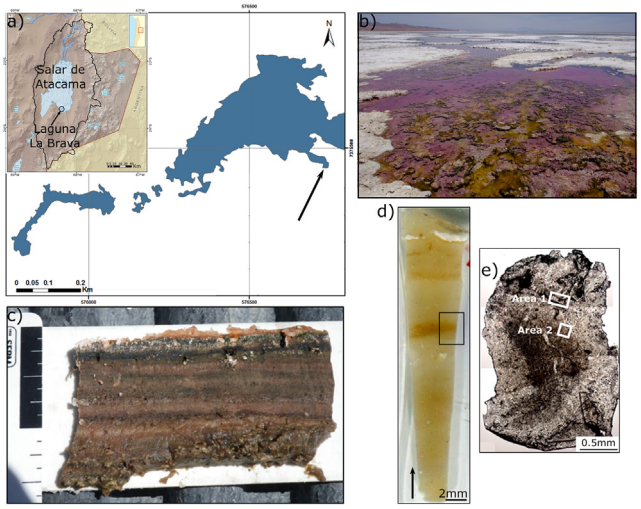

Fig. 1. Site location and view of the studied microbial mat from Laguna Brava, Salar de Atacama. (a) Aerial view of Laguna Brava showing the sampling site (inset from the Dirección General de Aguas website)). (b) Sampling site at Laguna Brava. (c) Photographs of a slice of the living microbial mat analyzed in this study. (d) Section of the microbial mat embedded in LR white (black box represents the analyzed zone shown in e). The arrow indicates the direction of growth. (e) 100 μm-thick polished section of the microbial mat. The two white boxes correspond to the two areas (area 1 and area 2) investigated using synchrotron techniques.

diel temperature fluctuations (air temperature fluctuates seasonally from −10 °C to 35 °C) and high arsenic concentrations (> 200 μM).

The microbial mats studied in this work are located at the southeastern shoreline of Laguna Brava (Fig. 1a), in a shallow (a few centimeters deep) channel that feeds groundwater into the lake. The microbial mats were sampled and immediately wrapped in PVDC plastic, transported to the lab in plastic containers and stored in the dark at 4 °C.

2.2. Water chemistry

The pH and the temperature were measured using a Metter-Toledo GoFive handheld pH/temperature probe. The conductivity and the salinity were determined with a Fisher Accumet AP75 handheld conductivity/temperature probe. Three replicas of water samples were taken ca. 5 cm above the mat and stored in glass vials (4-ml vials either under in situ pH conditions, acidified for analysis of major ions or fixed in 1.25 mM EDTA 87 mM acetic acid to determine the arsenic concentration). The water samples were kept refrigerated while being transported to the laboratory. Major cation (NH_4^+, K^+, Mg^{2+} and Ca^{2+}) and anion (SO_4^{2-} and NO_3^-) concentrations were determined by ion chromatography (Dionex ICS 3000) (Pace et al., 2018). Sulfide ($H_2S/HS^-/S^{2-}$) concentrations were measured using a microelectrode (Unisense, for details of the procedure for measuring the arsenic and sulfur compounds, see Sforna et al. (2017) and Pace et al. (2018)). The physicochemical composition of the water, given in Table 1, represents the average composition of the three water samples.

2.3. Mineralogical and elemental analysis

2.3.1. X-ray diffraction (PXRD)

The mineral composition was determined by powder X-ray diffraction. Finely grounded powder of fresh and dried (40 °C/24 h) samples were analyzed using a Panalytical X'per MPD diffractometer with copper anode (Cu Ka radiation). The diffraction patterns were collected from 5 to 80° (2θ) and analyzed with the program XPowder (Martin, 2004) and the database ICDD-PDF2. The patterns obtained from fresh

Table 1
Physicochemical properties of the water column at the sample locality.

Physicochemical prop.	Laguna Brava
pH	8.0 ± 0.1
Temperature air (°C)	7.9 (m.)- 23.7 (a.)
Temperature water (°C)	8.0 (m.)- 18.7(a.)
Alkalinity (mg/L)	685.5 ± 12.0
Conductivity (mS/cm)	99.0 ± 1.1
Salinity (g/L)	71
Light intensity (uE/m^2s)	78 (m.) - 1654 (a.)
Arsenic (μM)	206.8 ± 7.6
Sulfide (μM)	103.9 ± 3.1
Sulfate (mM)	40.8 ± 1.1
Nitrate (μM)	21.7 ± 1.5
Ammonium (μM)	74.7 ± 7.6
Magnesium (mM)	122.3 ± 2.1
Calcium (mM)	20.7 ± 2.1
Potassium (mM)	155.3 ± 3.1

*Measurements labelled m. or a. correspond to early morning or afternoon measurements, respectively.

and dried samples are shown in Fig. SI1.

2.3.2. Microscopy SEM-EDX

Sample section of fresh microbial mats of about 2 × 1 × 0.5 cm^3 dimensions were cut perpendicularly to the lamination (Fig. 2), fixed on an aluminum stub holder and sputtered with carbon. The samples were observed under vacuum using a Zeiss EVO SEM equipped with an Energy Dispersive Spectrometer (Bruker) using a voltage of 15 keV and a current beam of 2 nA. Spectra were analyzed using the software Quantax 200 (Bruker).

2.3.3. Major and trace element analysis

The major and trace element composition of the portion of mat investigated using synchrotron X-ray microfluorescence were analyzed at the *Services d'Analyses des roches et des Minéraux* (SARM) *du Centre de Recherches Pétrographiques et Géochimiques* de Nancy, France (Table 2). Major and trace elements were measured by ICP-OES and ICP-MS, respectively. The uncertainties are 5% for concentrations > 10 ppm and 15% for concentrations between 10 and 1 ppm (see Carignan et al. (2001) for a detail description of the experimental protocols use at SARM for major and trace element analyses).

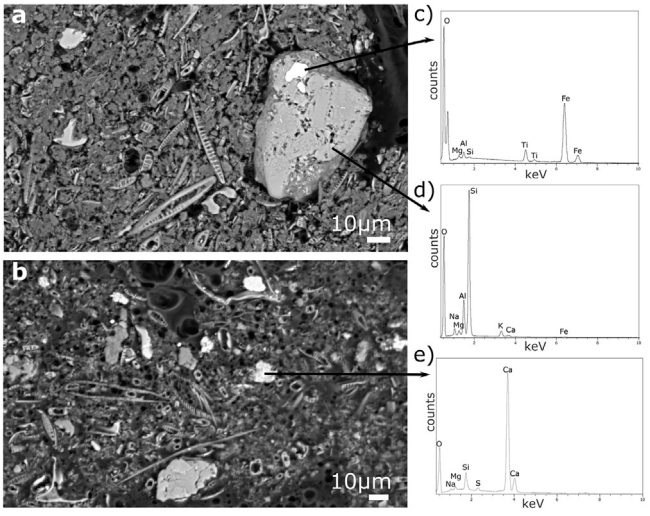

Fig. 2. Representatives SEM images (left) of the studied microbial mat showing the mineralogy, diatoms and other organisms embedded into an organic material. EDX analysis (right) of (c) iron-, (d) silicate- and (e) calcium-bearing phases.

Table 2
Bulk major and trace element concentrations of the Laguna Brava mat.

Sample	Concentration
Major oxide (%)	
SiO_2	29.1
CaO	11.0
Na_2O	7.8
MgO	6.3
K_2O	1.3
Al_2O_3	0.3
Fe_2O_3	0.1
LOI	44.1
Trace element (ppm)	
Sr	1360.0
As	330.5
Ba	53.8
Mo	48.4
Cu	28.8
Rb	24.9
Ge	12.0
Cl > Zn > V	< 10
Corg > Zr > Pb > Cr	< 5

*LOI = Loss-on-ignition. It represents the fraction associated to water and organic matter.

2.3.4. Confocal laser scanning microscopy analysis

The thin section of Fig. 1e was examined using an Olympus FluoView FV1000 CLSM characterized by a spectral resolution of 2 nm and a spatial resolution of 0.2 μm. An additional section of the fresh mat investigated was also observed. For examination of the later, an oil immersion objective UPLSAPO 60XO (Olympus; 60 magnification, numerical aperture 1.35) was used. For both samples, fluorescence stack images were obtained with a concomitant excitation at wavelengths of 405, 488 and 543 nm by collecting the emitted fluorescence between 425–475, 500–530 and 560–660 nm. Fluorescence spectra were acquired by collecting the emitted fluorescence between 435 and 796 nm, with bandwidth analyses of 10 nm and step size of 5 nm. The images were visualized and processed using the F10-ASW FLUOVIEW software (Olympus). The samples were investigated following the protocol described by Gérard et al. (2013).

2.4. Synchrotron analysis

For synchrotron analysis, microbial mats were progressively dehydrated in a series of ethanol baths (30%, 50%, 70%, 90% and 100%) and then gradually impregnated with hard grade LR-white resin (for details on the protocol, see Gérard et al. (2013)). This resin has a strong resistance to prolonged light exposure inherent to imaging and is free of metallic impurities. Petrographic thin sections were cut with a diamond wire saw and polished down to a homogenous thickness of ~100 μm (Fig. 1e). All synchrotron analyses were performed at the Nanoscopium beamline, SOLEIL synchrotron facility, France (Somogyi et al., 2015). The sample was raster scanned in a focused X-ray beam while measuring the emitted secondary radiation and/or the transmitted beam at each position. This allows simultaneous measurement of complementary contrast mechanisms including X-ray fluorescence, absorption, phase, and dark field revealing sample composition, chemistry and structure. The spatial resolution is determined by the beam-size and the experimental conditions and is typically between μm and a few tens of nanometers.

2.4.1. X-ray micro-fluorescence (μXRF)

A monochromatic incident X-ray beam was focused into a 2 × 2 μm^2 FWHM spot (Full Width at Half Maximum) at the sample position by using Kirckpatrick-Baez (KB) mirrors. The incident beam energy, 12 keV, was chosen by a double-crystal Si(111)

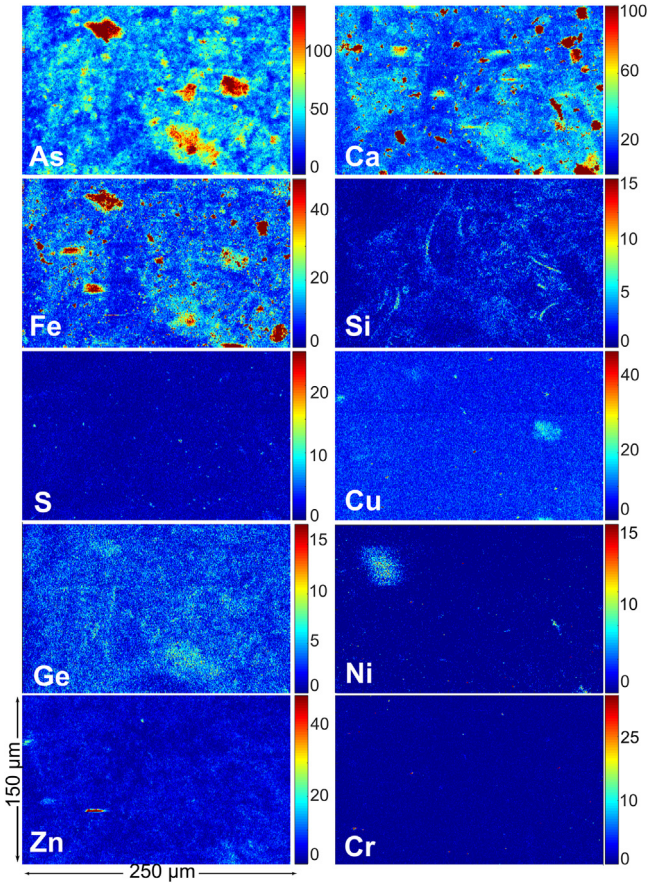

Fig. 3. XRF maps of area 1 of Fig. 1e showing the distribution patterns of As, Ca, Fe, Si, S, Cu, Ge, Ni, Zn and Cr. The colored scale indicates the background intensity (blue, below detection limit) and the maximum measured intensity (red). Dimension of the map is 250 µm × 150 µm. Mapping was performed using a 0.5 µm × 0.75 µm incremental step. (For interpretation of the references to colour in this figure legend, the reader is referred to the web version of this article.)

monochromator, just above the As K-edge for XRF imaging. At this energy, the measured photon flux in the 300 × 300 nm^2-sized focused beam was ~2 × 10^{10} photons/s. The sample was mounted onto a 3-axis sample positioning stage. The X-ray fluorescence radiation emitted by the sample was recorded by two identical silicon drift detectors of 50 mm^2 active surfaces (KETEK H50, KETEK GmbH) used with XMAP (XIA LLC) fast digital multichannel analyzer cards. The detectors were placed at backscattering geometry at ~100° compared to the incoming X-ray beam (at ~10° compared to the sample surface) (Somogyi et al., 2015). Elemental distribution maps (Fig. 3) were reconstructed from the XRF spectra by using preselected spectral regions of interest (ROIs) and summing the intensities measured by the two detectors (Bergamaschi et al., 2016) (Fig. SI2a). A deconvolution procedure using PyMCA (Solé et al., 2007) was applied to regions of the X-ray spectrum showing X-ray peaks overlap. The transmitted X-ray beam was recorded by a 300 µm-thick Si diode placed behind the sample, providing information about the morphology of the sample.

2D elemental distribution and transmission contrast maps were measured in two different areas. The first map consists of a 250 × 150 $µm^2$ large area measured using a resolution step of 0.5 × 0.75 $µm^2$ and 20 ms per point dwell time. The second map was obtained on a 140 × 140 $µm^2$ area using a 0.5 × 0.5 $µm^2$ resolution step and 30 ms per point dwell time. In order to compare the elemental distribution maps measured with different dwell times, the two intensity maps were normalized using the incident X-ray intensities (I0) recorded for each pixel. Further data treatment was performed using Matlab.

2.4.2. X-ray absorption near edge structure (XANES)

Seven different pellets and mineral standards were used for calibrating the XANES analysis of arsenic. These include: arsenopyrite (AsFeS), orpiment (As_2S_3), fetiasite (As(III)-fet, $(Fe(II,III)Ti)_3(As(III)_2O_5)O_2$; As_2O_3 pellet (Sigma-Aldrich), arsenobetaine (Asbet, $C_5H_{11}AsO_2$), legrandit (As(V)-leg, $Zn_2(As(V)O_4)(OH)\cdot(H_2O)$) and As_2O_5 pellet (Sigma-Aldrich). Micro-XANES measurements were performed in several spots of the mat sample.

XANES spectra were collected by scanning the energy using 0.5 eV steps around the K-edge of As in X-ray fluorescence and transmission modes. The beam energy was calibrated by defining the edge position of the legrandit and As_2O_5 standards at 11.8745 keV. The inflections points of the As K-edge XANES spectrum remained stable within 0.5 eV during the measurement period. To ensure the absence of photo-oxidation/reduction during synchrotron measurements, several As-XANES spectra were collected successively as a function of time in some selected points of the sample. No changes in these successive XANES spectra have been detected.

In order to determine the spatial variation of the speciation of arsenic in the sample, several "characteristics" X-ray energies were defined for XANES mapping. These X-ray energies correspond to the white lines of the XANES spectra of FeAsS, As_2S_3, As_2O_3, Asbet and As_2O_5 standards. In addition, three additional energy points were selected, corresponding to the pre- and far away As K-edge, and a medium energy point between Asbet and As_2O_5 standards. The resulting excitation energies (11.8653, 11.8684, 11.8696, 11.8714, 11.8727, 11.8745 and 11.8819 keV) allowed tracking the variations of arsenic speciation in the sample (Fig. SI2b). For each incident X-ray energy, a XRF map was obtained, representing a total of 7 X-ray maps for each selected zone of measurements. The obtained As speciation maps were treated with Matlab software. Only As_2O_3, [As(III)], and As_2O_5, [As(V)], maps are shown here for clarity (Fig. 4).

2.4.3. Principal Component Analysis (PCA) and clustering

The elemental intensities obtained from the XRF spectra were further analyzed by Principal Component Analysis (PCA) in an unsupervised manner for data reduction to identify quantitatively the dominant modes of metal associations and spatial distributions. The

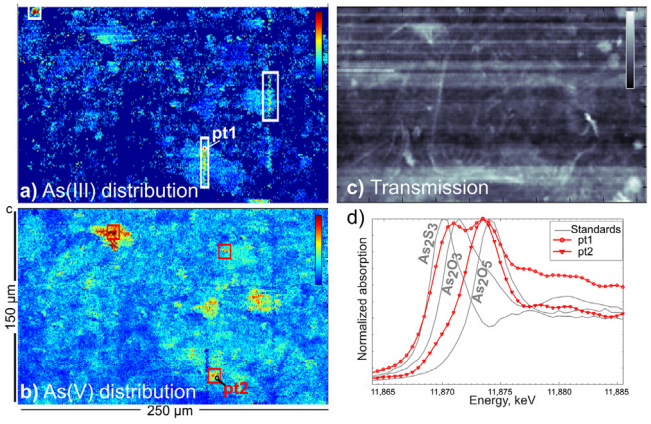

Fig. 4. XANES maps of (a) As (III) dominant region and (b) As(V) dominant region of the area 1 of Fig. 1e. The colored scale indicates the background intensity (blue) and the maximum intensity (red). The white (in a) and red (in b) boxes show regions where As(III) or As(V) predominates, respectively. (c) Reconstructed transmission map of the area 1 of Fig. 1e. The scale indicates low absorption/high transmission (black) and high absorption/low transmission (white). (d) XANES spectra at the As K-edge obtained in two representative areas where either As(III) (point 1 in panel a) or As(V) (point 2 in panel b) is most abundant. The three grey curves correspond to As_2S_3, As_2O_3 and As_2O_5 standards.

principal components are linear combinations of the original elemental intensities, along which the variation in the data is maximal. In order to treat all the variables (chemical elements) on the same basis, Singular Value Decomposition (SVD) was used to obtain the normalized eigenvectors of the correlation matrix. Clusters and scatterplots were derived to interpret the results of the multivariate analysis. The scores and loadings provide information about the measured sample pixels and the elements in the principal component space, respectively. Since PCA is designed to identify directions with the largest variation, it is not adapted for the identification of groups describing small sample variance. In the present case, the method was well-suited for discarding several variables and obtaining a final multivariate analysis with the chemical elements most linked with arsenic (Ca, S, Si and Fe).

PCA and clustering were performed on elemental data of area 1 (Fig. SI3 and tables SI from T1 to T3). Additional clustering was performed on the arsenic speciation maps obtained by XANES-imaging of area 2 (see clustering in Fig. 6b).

3. Results

3.1. Geochemical characteristics

The studied microbial mats are located in a channel supplying water to the lake (Fig. 1a). The water passing through this channel is associated with deposits of carbonate mounds, carbonate muds and diatomites (Boutt et al., 2016). The mats occur as continuous pink layers overlain by a 10 cm thick water column at the time of sampling (Fig. 1b). In cross section, the mats show a laminated structure composed of alternating green, purple, black and sporadically grey colored layers (Fig. 1c). The thickness of the layers varies with depth, and the deeper layers underline the progressive diagenetic alteration of the microbial mat through microbial and physicochemical processes. SEM images show that these mats are mainly composed of minerals, diatoms and prokaryotic microorganisms embedded into an organic exopolymeric material (Fig. 2).

At the time of sampling, the pH of the water column at the sample location was 8.0 ± 0.1, the water temperature was 8.0–18.7 °C during the early morning and mid-afternoon, respectively, and the salinity was 71 g/L. Noteworthy were the high arsenic (206.8 ± 7.6 μM) and sulfide ($H_2S/HS^-/S^{2-}$) (103.9 ± 3.1 μM) concentrations in the water column (Table 1). In addition, sulfide concentration in the porewater retrieved from the mat showed values between 104 and 234 μM (Supplementary Table 4). The ratio of major ions in the water column was $SO_4^{2-} > NO_3^-$ for anions and $K^+ > Mg^{2+} > Ca^{2+}$ for cations (Table 1).

3.2. Mineralogy

PXRD analysis showed that aragonite was the main phase with minor contributions of gypsum, quartz and a poorly crystalline phase attributed to iron oxides. In dried samples, halite, sylvite and part of the gypsum precipitated due to evaporation of the residual water trapped in the fresh sample (Fig. SI1). Quartz can be related to the diatoms present at the surface of some microbial mats in this lake and to the siliciclastic deposits present at Salar de Atacama (Corenthal et al., 2016). Gypsum crystals may have been transported by the wind from the surrounding evaporites and trapped by the mat, and/or directly precipitated in the microbial mat (e.g., Farías et al. (2014)). The detected aragonite was interpreted to be mainly authigenic since no calcite was present in the sample that was inspected. EDX measurements confirmed calcium carbonate phases obtained by PXRD and the presence of Si and O, in high-Si content minerals and diatom frustules observed by SEM-EDX. A phase composed of iron oxides was also detected. This phase could correspond to the poorly crystalline phase observed in the PXRD patterns.

3.3. Major and trace element chemistry

The average major and trace elements of Laguna Brava mats are represented in Table 2. Laguna Brava microbial mats were mainly composed of organic matter as indicated by a 44% loss on ignition. The major elements detected include Si, Ca, Na, Mg, K, Al, Fe and Sr, which is consistent with the composition of the groundwater (Boutt et al., 2016). The high concentration of arsenic carried throughout the water column was reflected in the relatively high abundance of this element in the sample (330 ppm). Other abundant trace elements include Ba, Mo, Cu, Rb and Ge (between a range of 50 and 10 ppm) followed by Cl, Zn and Cr (< 10 ppm).

Two main areas (area 1 and area 2) were selected for μ-XRF and μ-XANES mapping and in situ analyses (Fig. 1e). These areas were chosen based on previous fast-acquisition, poorly-resolved maps obtained in different zones of the samples. These two areas show contrasted mineral-organic regions as well as localized hot spots of arsenic. Fig. 3 shows the element distribution maps of As, Ca, Fe, Si, S, Cu, Ge, Ni, Zn and Cr of area 1. Although low Z elements such as Si, Cl and S display relative intense X-ray peaks, their information depth, which corresponds to the mean free path of the fluorescence photons in the mat-based matrix, is significantly smaller (~50 μm) than the total thickness of the sample (100 μm). Accordingly, these elements are underestimated compared to high Z elements such as Fe, Zn, Cr and As. Si displayed a fiber-shaped distribution map, which is best attributed to diatoms. In contrast, S, Zn and Cr occurred as hotspots, while Cu and Ni appeared locally enriched. Despite a low intensity signal, Ge showed a similar pattern as As. ICP-MS analysis highlighted the presence of other elements such as Sr, Mo and Rb. However, these high Z elements were not detected using the experimental protocol used at Nanoscopium.

3.4. Inter-correlation of elements with arsenic

PCA was first performed using the different elements detected in area 1. The correlation values obtained (i.e. percentage of the variability in the data) were too low to provide meaningful inter-correlation patterns. For this reason, we chose to focus the PCA analysis on the most abundant elements, that is Si, S, Ca, Fe and As. The contribution of each PC to the total signal appears relatively small (between 16 and 25%, see Tables S2), which is best attributed to the strong heterogeneity of the system. For this reason, five different PC's were necessary to describe the compositional variation of the sample (Tables S2 and S3).

Three important observations emerged from the PCA. First, that a part of Ca appeared linked to S, second, that Si did not show any particular association to other elements and third and most importantly, that As only partially correlated with Fe. In order to visualize the distribution of data reduction, clustering was used, which provides an “assumption-free” analysis of the distribution of chemical components in the sample by classifying pixels according to their spectral similarity (Etschmann et al., 2014). The four clusters shown in Fig. SI3b summarize the most striking features of the sample analyzed. In particular, the specific contribution of Ca and Fe (cluster 1), zones with a high contribution of arsenic (cluster 2), fiber-shaped Si distribution likely reflecting the shape of diatoms (cluster 3), and zones with a high contribution of sulfur (cluster 4). In order to further investigate the spatial distribution relationship between Fe and As shown by the PCA, scatter plots were derived from cluster 1 (Ca and Fe contributions) and cluster 2 (high As contribution) (Fig. 5). Scatter plots provide a qualitative indication of the degree of co-localization (Dunn et al., 2011). In addition, to illustrate the significance of both scatter plots, distribution maps of As and Fe of both cluster 1 and cluster 2 were also derived (Fig. 5c–f). Scatter plot of cluster 1 showed a bimodal distribution defined as ‘A’ and ‘B’ in Fig. 5a. Distribution ‘A’ correspond to the domains of the map containing mainly Fe with little or only minor contribution from As (compare Fig. 5c and e). Distribution ‘B’ reflected the spatial

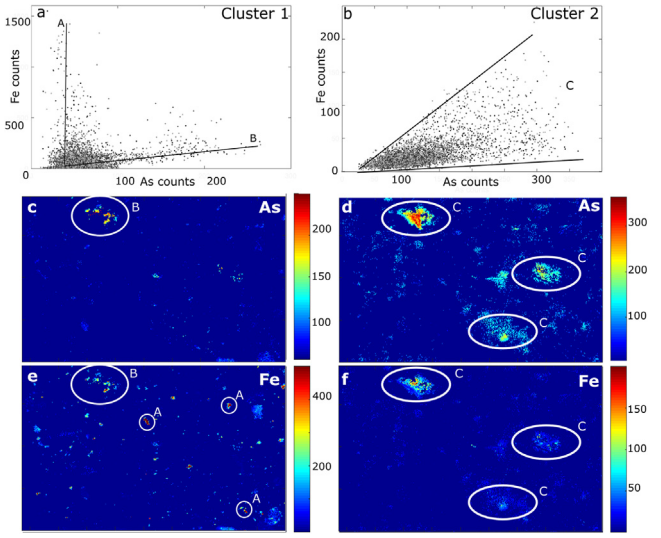

Fig. 5. Co-localization of As and Fe in area 1 of Fig. 1e. Scatter plots of As and Fe intensities of cluster 1 (a) and cluster 2 (b), and associated element distribution maps of cluster 1 (c, e) and cluster 2 (d, f). Note the bimodal distribution of As and Fe in cluster 1 (a) and the linear relation of As and Fe in cluster 2 (b). In cluster 1, several domains where Fe is not overlapping with As are shown with the circles labelled 'A' in panel e. The domains where As and Fe are overlapping are shown with circles labelled 'B' (in cluster 1, panels c and e) and 'C' (in cluster 2, panels d and f). The total clusters 1 and 2 are shown in Supplementary Fig. SI3.

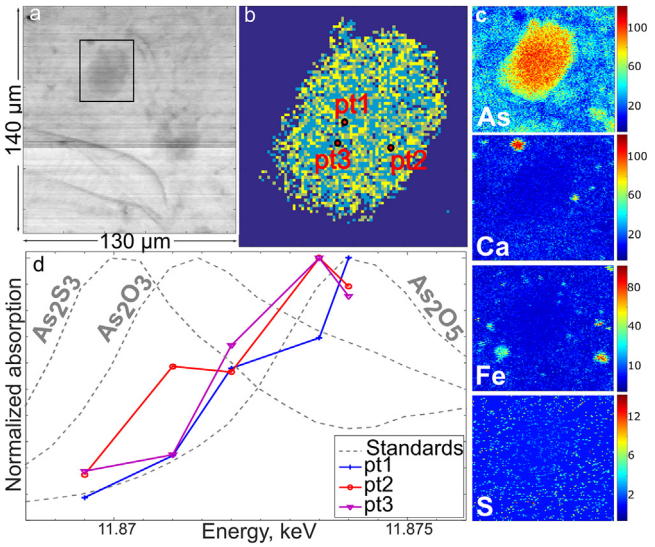

Fig. 6. (a) Transmission image of the area 2 of Fig. 1e showing diatoms and a low absorption organic-rich globule (framed grey area). (b) Composite cluster image of the As speciation distribution of the boxed area in (a). (c) Maps of As, Ca, Fe and S distribution patterns of the boxed area in (a). Note the high concentration of As and the absence of Ca, Fe and S in the globule-like domain. (d) Variation of As intensity at the As K-edge extracted from the XANES image stacks in randomly selected spots (pt1, pt2 and pt3 shown in panel b) revealing the high spatial heterogeneity of the As speciation. The three grey curves represent As_2S_3, As_2O_3 and As_2O_5 standards.

overlap between As and Fe. In contrast to the scatter plot of cluster 1, the scatter plot of cluster 2 displayed a single linear distribution ('C', in Fig. 5b) characterized by a relatively large range of Fe and As concentrations. This diffuse pattern is well illustrated in Fig. 5d and f. As shown in Fig. 4 and discussed below, it is worth emphasizing that the As (V) is the main contributor to the distribution maps shown in Fig. 5 and that As(III) represents only a minor component of the system.

3.5. Speciation of arsenic compounds

The resulting maps of As(III) and As(V) revealed that As(III) displayed a fiber-shaped pattern, while As(V) appeared either as small, near-circular spots or as diffuse domains across area 1 (Fig. 4). Ten different XANES spectra collected in representative domains of area 1 showed different apparent proportions between As(III) and As(V). In As (III) dominant domains, As(III) was always found together with As(V). In contrast, in As(V) dominant domains, As(V) occurred as the main constituent, with little or no contribution from As(III) (Fig. 4).

Elemental association analysis performed for area 2 (Fig. 1e) revealed that As was the main element present in a 30 µm large oval-shaped globule (Fig. 6c). This globule was characterized by a low absorption signal in the X-ray transmission image (Fig. 6a), indicating the potential presence of organic material. Specifically, the Laguna Brava microbial mat was mainly composed of exopolymeric substances (EPS; i.e., soft organic tissue, or slime) (Dupraz and Visscher, 2005), which are characterized by lower absorption coefficients. The occurrence of large amounts of EPS in the mat was further supported by CLSM analysis. As shown in Fig. 7, the fluorescence emission with a maximum at 470 nm of the 30 µm large oval-shaped globule appeared similar to the one obtained in the EPS and remnant sheaths of the fresh mat. This suggests that the main component forming the oval-shaped globule was organic material. In order to further constrain the As distribution and co-variation patterns in this globule, additional PCA and cluster analysis were performed on the arsenic speciation data. Results showed a marked heterogeneous distribution and high spatial heterogeneity of As speciation (Fig. 6b), even at a 500 nm resolution. In addition, the

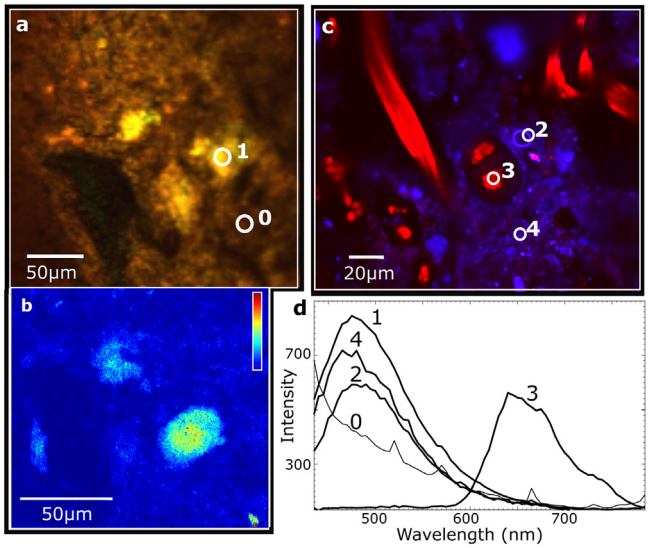

Fig. 7. (a) Fluorescence map emitted in the range 435–796 nm following an excitation at 405 nm of the boxed area shown in Fig. 6a. (b) XRF map showing the distribution of As in the same area of (a). Fluorescence intensity is shown on the blue-red colored scale. (c) Fluorescence map emitted in the range 435–796 nm following an excitation at 405 nm in a fresh section of the studied microbial mat. (d) Fluorescence emission spectra obtained with an excitation at 405 nm on an As-rich globule (white circle labelled 1 of panel a), a sheath (white circle 2 of panel c), a possible cyanobacteria (white circle 3 of panel c) and the EPS (white circle 4 of panel c). The white circle labelled 0 of panel a) corresponds to the background spectrum labelled 0 of panel d). (For interpretation of the references to colour in this figure legend, the reader is referred to the web version of this article.)

variation of the As intensity as a function of the characteristic X-ray energies that were applied is shown in some randomly chosen sample spots within this sample area (Fig. 6d).

4. Discussion

4.1. Arsenic immobilization in Laguna Brava mats

Arsenic species can be immobilized in mats by sorption or incorporation in minerals, such as Fe, Mn or Al (oxy)hydroxides, sulfates or carbonates, or by incorporation into the exopolymeric substances (Sforna et al., 2017). Together with microbial-induced arsenic reactions, the occurrence of these three processes is likely to control the cycling of arsenic species in microbial mats. In reducing conditions, where elevated As and S concentrations prevail, precipitation of arsenopyrite or As-bearing pyrite can be expected (e.g. Craw et al., 2003). Although the distribution of (total) sulfur could not be observed in the XRF analysis due to its low XRF energy line, the high concentration of sulfur in the water column, and porewater of the mat, suggests that S-bearing compounds (i.e., sulfide, thiosulfate and polysulfide) could be abundant in these mats. Neither pyrite nor Fe-S phases were detected by EDX or XRD. In addition, reduced As(0) associated with arsenopyrite formation was not identified in the XANES analysis. The lack of pyrite or other crystallized Fe-bearing phases strongly suggests that sulfur is present in the EPS as S-functional groups, such as sulfinic and thiol, or polysulfides (Braissant et al., 2007). Furthermore, arsenic-sulfide complexes can be formed through the interaction of arsenic with S-functional groups present in the EPS (Sforna et al., 2017), or from products of microbial metabolisms such as in *Pyrobaculum yellowstonensis* (Jay et al., 2015). This chemoorganoheterotroph reduces arsenate and sulfur, resulting in the abiotic formation of monothioarsenate, dithioarsenate and polysulfide. This indicates that As-S compounds may be an important sink for arsenic in Laguna Brava mats. Further experiments on the same samples at the absorption edge of sulfur are required to document the spatial distribution and speciation of sulfur.

Our results show that As is not linked to Ca, Si nor Mn, and only moderately linked to Fe. This suggests that none of the main mineral phases present in Laguna Brava mats (i.e., aragonite, gypsum and quartz) appeared to contain arsenic in their structure. However, arsenic can be incorporated into gypsum (Fernández-Martínez et al., 2006), which occurs either as direct precipitate in the mat or as an exotic phase derived from aeolian input. Calcite can retain trace elements on its surface via adsorption reactions or through co-precipitation reactions (Renard et al., 2015). But, only aragonite was detected in Laguna Brava mats and the interaction between As and aragonite has not yet been investigated in detail. As shown by Smedley and Kinniburgh (2002) and Borch et al. (2010), arsenic has a strong capacity of adsorption onto iron (oxy)hydroxide minerals. Absorption on (oxy)hydroxide phases is mainly controlled by temperature, pH, redox potential, nature of the As species, competition with other species, as well as the surface area, morphology and charge of the solid surface (e.g. Santini and Ward, 2012). For each mineral, there is a unique 'zero point of charge', called pH_{ZPC}, which corresponds to the pH at which the surface is not charged and therefore is not able to adsorb trace metals. Solid surface are positively charged below their pH_{ZPC} and, conversely, negatively charged above this value (e.g. Santini and Ward, 2012). Under slightly alkaline pH (8.0 ± 0.1) of Laguna Brava, most iron (oxy)hydroxide minerals are negatively charged, and thus the also negatively-charged arsenic oxyanions should not sorb onto their surface. However, ferrihydrite, Fe$(OH)_3$, a common iron oxyhydroxide, has a high enough pH_{ZPC} ~8 to remain positively charged in mild alkaline conditions (Pivovarov, 2009). Moreover, ferrihydrite has a large surface area compared to other iron (oxy)hydroxide minerals, which increases its affinity for the sorption of As oxyanions (Langmuir, 1997; Ravenscroft et al., 2009). Iron (oxy)hydroxides are strong adsorbers of As(V) oxyanions and to a lesser extent As(III) oxyanions (e.g. Fuller et al. (1993), Zobrist et al. (2000) and Smedley and Kinniburgh (2002)). The iron (oxy)hydroxide mineral identified by EDX, and XRD diffractograms displays a poorly-ordered structure, which matches the observed Fe$(OH)_3$ diffraction pattern (Fig. SI1). Accordingly, we suggest that the only potential mineral that may have sorbed arsenic in the mat is probably ferrihydrite. This is supported by the scatter plots and distribution maps of As and Fe derived from clusters 1 and 2 of area 1 (Fig. 5), which show that As correlates proportionally with Fe (Fig. 5a). This correlation can be seen in hotspots of < 10 μm in diameter (Fig. 5c), which supports the interpretation that As is sorbed onto microscopic Fe-bearing minerals.

In addition to mineral sorption, As can also be immobilized in the microbial mat by interaction with functional groups present in the organic matrix of the EPS, such as carboxyl, phosphate, amino, or the previously mentioned sulfur groups (Decho et al., 2005). The functional groups of the EPS deprotonate as a function of pH, and will provide a negative charge to the EPS at alkaline values (Braissant et al., 2007). The interactions with positively charged ions, including Ca^{2+} and Mg^{2+} but likely also $Fe^{2+/3+}$, can form bidentate bonds with low-molecular-weight organic carbon (Braissant et al., 2009), or likely with negatively charged ions, such as arsenic oxyanions. The cation sorption at the surface of the mat is suggested to be a non-specific and abiologically-induced (passive sorption) process, thus promoting homogenous metal(loid) distribution in the top layers of the mat (Sforna et al., 2017). As the microbial mat grows, aerobic and anaerobic heterotrophs will consume ca. 10% of the EPS per day (Decho et al., 2005), which in turn can be accompanied by the release of the metal(loid)s trapped at the surface of the mats (Sforna et al., 2017). Although difficult to confirm without further ultra-high resolution investigations at the atomic scale (e.g., using transmission electron microscopy), the As-Fe distribution pattern shown in Fig. 5d may reflect release of both As and Fe molecular compounds attending EPS degradation. Specifically, the diffused distribution pattern of As and Fe shown in the scatter plot of Fig. 5b and associated elemental map of Fig. 5d and f, could be attributed to As/Fe desorption from the EPS.

4.2. Arsenic speciation in Laguna Brava mats

The heterogeneous distribution of As(III) and As(V), either together or separately, in specific confined areas of the mats suggests that a specific process was at play. Given the environmental conditions prevailing at Laguna Brava, i.e., mild alkaline pH (8.0 ± 0.1) and low reduction potential (−100 to −350 mV), uncharged arsenite (H_3AsO_3) is expected to be the predominant chemical specie in the mats, followed by $HAsO_4^{2-}$ and $HAsO_3^{-}$ (Smedley and Kinniburgh, 2002). Assuming chemical equilibrium, this suggests that As(III) should be the dominant cation in the living mats. This is in stark contrast with our X-ray absorption results, which showed a much lower concentration of As(III) than that of As(V). The high sulfide concentration and absence of free-oxygen in the overlying water layer (Visscher et al., in prep.) argue against abiotic oxidation of arsenic within the mat. Arsenic speciation can change as a result of biological transformations and redox disequilibrium (e.g., Zhu et al., 2014). For instance, the As(V)/As(III) ratio in open seawater is typically of the order of 10 to 100, significantly higher than the 10^{15} to 10^{26} range that would be expected on the basis of thermodynamic equilibrium. This drastic difference is attributed to microbial activity (Andreae, 1979; Smedley and Kinniburgh, 2002). The mobility of the different As species is another critical factor to be considered. Arsenite is more mobile than arsenate and consequently, more likely to escape the mat along specific fluid conduits during natural compaction, dehydration and/or sampling of the mat. The specific enrichment of As(III) along linear features oriented nearly-perpendicular to the layering of the microbial mat (Fig. 4a) may reflect the preferential loss of As(III) during fluid escape along micro-desiccation cracks, pressure-induced micro-channels, or existing water channels in the EPS. The 3D structure (architecture) of the EPS may also facilitate the delivery of nutrients, enhance metabolic substrates to the biofilm community and, simultaneously, removal of toxic waste from the microbe community (Korber et al., 1993; Costerton et al., 1994; Decho et al., 2005). A fluid-induced process could also explain the late

precipitation of soluble phases detected in dried samples (Fig. SI1). Soluble ions such as SO_4^{2-}, Cl^-, Ca^{2+}, Na^+ or K^+ are important constituents of the pore-water trapped in the EPS matrix. Dehydration of (fresh) samples in the laboratory results in efflorescence that may have induced gypsum, halite and/or sylvite precipitation (Fig. SI1), and potentially the release of As(III).

4.3. Potential arsenic pathways in Laguna Brava mats

The results from fossilized Precambrian microbial mats (Sforna et al., 2014) and modern analogues from the Bahamas (Sforna et al., 2017), suggest that the 40 μm-diameter organic-rich globule containing arsenic but no other trace metals (Figs. 6 and 7) could be a biological-mediated As enrichment. The occurrence of both As(III) and As(V) oxidation states at the microscopic scale in this organic globule argues for a microbially-mediated cycling of arsenic. Different As-based metabolic processes have been documented. Most of these are closely related to known sulfur- and sulfide-oxidizers, as well as sulfur- and sulfate-reducers. For instance, As(III) can be used as an electron donor for phototrophy or chemolithotrophy, and As(V) as an electron acceptor for anaerobic chemoorganotrophic respiration or chemolithotrophically with H_2S. Recently, Hoeft et al. (2016) reported three strains of the purple-sulfur bacterium *Ectothiorhodospira* capable of anoxygenic photosynthesis using As(III) as electron donor. The strains were isolated from Mono Lake in California and Big Soda Lake in Nevada, both showing similarities to Laguna Brava setting (e.g., highly alkaline, hypersaline, considerable arsenic concentrations and the presence of purple sulfur bacteria). Hence, anoxygenic photosynthesis appears a viable metabolic pathway to explain the occurrence of As(III) and As(V) in the organic globule, although its localization a few mm below the surface may have strongly inhibited the penetration of light. Arsenite can also be oxidized chemolithotrophically in the presence of nitrate (Hoeft et al., 2007), or possibly other available electron acceptors such as chlorate (Sun et al., 2010). Sulfide oxidizers, which use either oxygen or nitrate to oxidize sulfide while fixing CO_2 (Visscher et al., 1992), are common in microbial mats (e.g. van Gemerden, 1993). *Alkalilimnicola ehrlichii*, a sulfide oxidizer capable of sulfide and As(III) oxidation using nitrate as an electron acceptor, has been isolated in Mono Lake (Hoeft et al., 2007). Sulfide oxidizers, represented by Gammaproteobacteria, have been reported in several saline ponds of the Atacama Desert (Thiel et al., 2010; Lara et al., 2012). Considering the high concentration of arsenic in Laguna Brava, it cannot be excluded that in addition to sulfide, these microbes used As(III) for respiration. The arsenate formed this way, can have been involved in a variety of metabolic pathways. Some species of Deltaproteobacteria are capable of arsenate respiration (Newman et al., 1997; Macy et al., 2000) and they have been reported in a variety of microbial mats from Laguna Brava and the nearby Laguna Tebenquiche (Farias et al., 2017). In addition, microorganisms capable of selenate respiration (e.g., *Bacillus selenitireducens*), belonging to the phylum Firmicutes can sometimes replace this oxyanion with arsenate (Oremland and Stolz, 2000).

Methylation processes could be also invoked in Laguna Brava mats. However, even if some microbes deploy methylation to detoxify arsenic, the involved reactions are still not well understood (Mukhopadhyay and Rosen, 2002; Couture et al., 2013; Kruger et al., 2013; Huertas et al., 2014; Hug et al., 2014). It has been suggested that methylation reactions may be used as an (supplementary) energy source (Yamamura and Amachi, 2014). This detoxification pathway is a multistep process of methylation and redox reactions followed by formation of organoarsenic intermediates, like arsenosugars or arsenolipids (Bentley and Chasteen, 2002; Mukhopadhyay and Rosen, 2002). Methylation reactions will release several compounds in a nearby location. This could explain the co-occurrence of As(III) and As(V) at a micrometer scale within the organic globule shown in Fig. 6. Further experiments using XANES standards of arsenic-methylated species are underway to clarify the potential for arsenic methylation in Laguna Brava mats.

4.4. Concluding remarks

A combination of conventional geochemical techniques, such as X-ray diffraction, SEM-EDX, CLSM and state-of-the-art synchrotron imaging techniques, including X-ray micro-fluorescence (μXRF) and X-ray Absorption Near Edge Structure (XANES) mapping, was used to investigate the relationship between minerals, trace metals, organic matter and microbial activity within microbial mats of Laguna Brava, a hypersaline lake with a high arsenic concentration in the Salar de Atacama (Chile). We have documented a number of features that support the biological cycling of arsenic. These include the incorporation of arsenic into EPS, the identification of organic-rich globules containing abundant arsenic with no other trace metals, and the heterogeneous distribution of As(III) and As(V), either together or separately and at different scales. Although accurate information on sulfur distribution and speciation are missing, the high concentration of both sulfur and arsenic in the water column supports the notion of a coupled arsenic-sulfur cycle. Additional experiments are required to better document the presence, and influence, of sulfur in the Laguna Brava mats. Our results also highlight how the multi-technique approach used in this work represents a powerful mean to unravel specific abiotic/biological processes at multi length-scale (100 nm to multiple-cm scale) in both modern and ancient rocks.

Acknowledgments

This work has received funding from the European Union's Horizon 2020 Research and Innovation programme under the Marie Skłodowska – Curie Grant Agreement No 701662 and the Programme National de Planétologie.

Appendix A. Supplementary data

Supplementary data to this article can be found online at https://doi.org/10.1016/j.chemgeo.2018.04.029.

References

Albarracín, V.H., Gärtner, W., Farias, M.E., 2016. Forged under the sun: life and art of extremophiles from Andean lakes. Photochem. Photobiol. 92, 14–28.
Andreae, M.O., 1979. Arsenic speciation in seawater and interstitial waters: the influence of biological-chemical interactions on the chemistry of a trace element1. Limnol. Oceanogr. 24, 440–452.
Bentley, R., Chasteen, T.G., 2002. Microbial methylation of metalloids: arsenic, antimony, and bismuth. Microbiol Mol Biol Rev 66, 250–271.
Bergamaschi, A., Medjoubi, K., Messaoudi, C., Marco, S., Somogyi, A., 2016. MMX-I: data-processing software for multimodal X-ray imaging and tomography. J. Synchrotron Radiat. 23, 783–794.
Borch, T., Kretzschmar, R., Kappler, A., Cappellen, P.V., Ginder-Vogel, M., Voegelin, A., Campbell, K., 2010. Biogeochemical redox processes and their impact on contaminant dynamics. Environ. Sci. Technol. 44, 15–23.
Boutt, D.F., Hynek, S.A., Munk, L.A., Corenthal, L.G., 2016. Rapid recharge of fresh water to the halite-hosted brine aquifer of Salar de Atacama, Chile. Hydrol. Process. 30, 4720–4740.
Braissant, O., Decho, A.W., Dupraz, C., Glunk, C., Przekop, K.M., Visscher, P.T., 2007. Exopolymeric substances of sulfate-reducing bacteria: interactions with calcium at alkaline pH and implication for formation of carbonate minerals. Geobiology 5, 401–411.
Braissant, O., Decho, A.W., Przekop, K.M., Gallagher, K.L., Glunk, C., Dupraz, C., Visscher, P.T., 2009. Characteristics and turnover of exopolymeric substances in a hypersaline microbial mat. FEMS Microbiol. Ecol. 67, 293–307.
Cabral, A.R., Beaudoin, G., 2007. Volcanic red-bed copper mineralisation related to submarine basalt alteration, Mont Alexandre, Quebec Appalachians, Canada. Mineral. Deposita 42, 901–912.
Cabrera, S., Pizarro, G., 1992. Changes in chlorophyll a concentration, copepod abundance and UV and PAR penetration in the water column during the ozone depletion in Antarctic Lake Kitiesh. Arch für Hydrobiol. 43, 123–134.
Carignan, J., Hild, P., Mevelle, G., Morel, J., Yeghicheyan, D., 2001. Routine analyses of trace elements in geological samples using flow injection and low pressure on-line liquid chromatography coupled to ICP-MS: a study of geochemical reference materials BR, DR-N, UB-N, AN-G and GH. Geostand. Newslett. 25, 187–198.

Corenthal, L.G., Boutt, D.F., Hynek, S.A., Munk, L.A., 2016. Regional groundwater flow and accumulation of a massive evaporite deposit at the margin of the Chilean Altiplano. Geophys. Res. Lett. 43, 8017–8025.
Costerton, J.W., Lewandowski, Z., DeBeer, D., Caldwell, D., Korber, D., James, G., 1994. Biofilms, the customized microniche. J. Bacteriol. 176, 2137–2142.
Couture, R.-M., Rose, J., Kumar, N., Mitchell, K., Wallschläger, D., van Cappellen, P., 2013. Sorption of Arsenite, arsenate, and Thioarsenates to Iron oxides and Iron sulfides: a kinetic and spectroscopic investigation. Environ. Sci. Technol. 47, 5652–5659.
Craw, D., Falconer, D., Youngson, J.H., 2003. Environmental arsenopyrite stability and dissolution: theory, experiment, and field observations. Chem. Geol. 199, 71–82.
Decho, A.W., Visscher, P.T., Reid, R.P., 2005. Production and cycling of natural microbial exopolymers (EPS) within a marine stromatolite. Palaeogeogr. Palaeoclimatol. Palaeoecol. 219, 71–86.
Dunn, K.W., Kamocka, M.M., McDonald, J.H., 2011. A practical guide to evaluating colocalization in biological microscopy. Am. J. Physiol. Cell Physiol. 300, C723–C742.
Dupraz, C., Visscher, P.T., 2005. Microbial lithification in marine stromatolites and hypersaline mats. Trends Microbiol. 13, 429–438.
Duval, S., Ducluzeau, A.-L., Nitschke, W., Schoepp-Cothenet, B., 2008. Enzyme phylogenies as markers for the oxidation state of the environment: the case of respiratory arsenate reductase and related enzymes. BMC Evol. Biol. 8, 206.
Etschmann, B.E., Donner, E., Brugger, J., Howard, D.L., De, Jonge M.D., Paterson, D., Naidu, R., Scheckel, K.G., Ryan, C.G., Lombi, E., 2014. Speciation mapping of environmental samples using XANES imaging. Environ. Chem. 11, 341–350.
Farías, M.E., Rascovan, N., Toneatti, D.M., Albarracín, V.H., Flores, M.R., Poiré, D.G., Collavino, M.M., Aguilar, O.M., Vazquez, M.P., Polerecky, L., 2013. The discovery of Stromatolites developing at 3570 m above sea level in a high-altitude volcanic Lake Socompa, Argentinean Andes. PLoS One 8, 1–15.
Farías, M.E., Contreras, M., Rasuk, M.C., Kurth, D., Flores, M.R., Poiré, D.G., Novoa, F., Visscher, P.T., 2014. Characterization of bacterial diversity associated with microbial mats, gypsum evaporites and carbonate microbialites in thalassic wetlands: Tebenquiche and La Brava, Salar de Atacama, Chile. Extremophiles: Life Under Extreme Conditions 18, 311–329.
Farias, M.E., Rasuk, M.C., Gallagher, K.L., Contreras, M., Kurth, D., Fernandez, A.B., Poiré, D., Novoa, F., Visscher, P.T., 2017. Prokaryotic diversity and biogeochemical characteristics of benthic microbial ecosystems at La Brava, a hypersaline lake at Salar de Atacama, Chile. PLoS One 12, 1–25.
Fernandez, A.B., Rasuk, M.C., Visscher, P.T., Contreras, M., Novoa, F., Poire, D.G., Patterson, M.M., Ventosa, A., Farias, M.E., 2016. Microbial diversity in sediment ecosystems (Evaporites domes, microbial Mats, and crusts) of Hypersaline Laguna Tebenquiche, Salar de Atacama, Chile. Front. Microbiol. 7, 1284.
Fernández-Martínez, A., Román-Ross, G., Cuello, G.J., Turrillas, X., Charlet, L., Johnson, M.R., Bardelli, F., 2006. Arsenic uptake by gypsum and calcite: modelling and probing by neutron and X-ray scattering. Phys. B Condens. Matter 385, 935–937.
Fuller, C.C., Davis, J.A., Waychunas, G.A., 1993. Surface chemistry of ferrihydrite: part 2. Kinetics of arsenate adsorption and coprecipitation. Geochim. Cosmochim. Acta 57, 2271–2282.
Gérard, E., Ménez, B., Couradeau, E., Moreira, D., Benzerara, K., Tavera, R., López-García, P., 2013. Specific carbonate–microbe interactions in the modern microbialites of Lake Alchichica (Mexico). ISME J. 7, 1997–2009.
Hoeft, S.E., Blum, J.S., Stolz, J.F., Tabita, F.R., Witte, B., King, G.M., Santini, J.M., Oremland, R.S., 2007. *Alkalilimnicola ehrlichii* sp. nov., a novel, arsenite-oxidizing haloalkaliphilic gammaproteobacterium capable of chemoautotrophic or heterotrophic growth with nitrate or oxygen as the electron acceptor. Int. J. Syst. Evol. Microbiol. 57, 504–512.
Hoeft, S.E., Boren, A., Hernandez-Maldonado, J., Stoneburner, B., Saltikov, C.W., Stolz, J.F., Oremland, R.S., 2016. Arsenite as an Electron donor for Anoxygenic photosynthesis: description of three strains of Ectothiorhodospira from mono Lake, California and big soda Lake, Nevada. Life 7 (1).
Huertas, M.J., López-Maury, L., Giner-Lamia, J., Sánchez-Riego, A.M., Florencio, F.J., 2014. Metals in cyanobacteria: analysis of the copper, nickel, cobalt and arsenic homeostasis mechanisms. Life 4, 865–886.
Hug, K., Maher, W.A., Stott, M.B., Krikowa, F., Foster, S., Moreau, J.W., 2014. Microbial contributions to coupled arsenic and sulfur cycling in the acid-sulfide hot spring champagne pool, New Zealand. Front. Microbiol. 5, 569.
Jay, Z.J., Beam, J.P., Dohnalkova, A., Lohmayer, R., Bodle, B., Planer-Friedrich, B., Romine, M., Inskeep, W.P., 2015. *Pyrobaculum yellowstonensis* strain WP30 respires on elemental sulfur and/or arsenate in circumneutral sulfidic geothermal sediments of Yellowstone national park. Appl. Environ. Microbiol. 81, 5907–5916.
Korber, D.R., Lawrence, J.R., Hendry, M.J., Caldwell, D.E., 1993. Analysis of spatial variability within mot + and mot- pseudomonas fluorescens biofilms using representative elements. Biofouling 7, 339–358.
Kruger, M.C., Bertin, P.N., Heipieper, H.J., Arsène-Ploetze, F., 2013. Bacterial metabolism of environmental arsenic-mechanisms and biotechnological applications. Appl. Microbiol. Biotechnol. 97, 3827–3841.
Langmuir, D., 1997. Aqueous environmental geochemistry. Prentice Hall, Upper Saddle River, NJ.
Lara, J., González, L., Ferrero, M., Díaz, G., Pedrós-Alió, C., Demergasso, C., 2012. Enrichment of arsenic transforming and resistant heterotrophic bacteria from sediments of two salt lakes in northern Chile. In: Extremophiles: Life Under Extreme Conditions. 16. pp. 523–538.
Lebrun, E., Brugna, M., Baymann, F., Muller, D., Lièvremont, D., Lett, M.C., Nitschke, W., 2003. Arsenite oxidase, an ancient bioenergetic enzyme. Mol. Biol. Evol. 20, 686–693.
Lièvremont, D., Bertin, P.N., Lett, M.-C., 2009. Arsenic in contaminated waters: biogeochemical cycle, microbial metabolism and biotreatment processes. Biochimie 91, 1229–1237.
Macy, J.M., Santini, J.M., Pauling, B.V., O'Neill, A.H., Sly, L.I., 2000. Two new arsenate/sulfate-reducing bacteria: mechanisms of arsenate reduction. Arch. Microbiol. 173, 49–57.
Martin, J.D., 2004. Using XPOWDER: A Software Package for Powder X-ray Diffraction Analysis.
Mukhopadhyay, R., Rosen, B.P., 2002. Arsenate reductase in prokaryotes and eukaryotes. Environ. Health Perspect. 110, 745.
Newman, D.K., Kennedy, E.K., Coates, J.D., Ahmann, D., Ellis, D.J., Lovley, D.R., Morel, F.M., 1997. Dissimilatory arsenate and sulfate reduction in *Desulfotomaculum auripigmentum* sp. nov. Arch. Microbiol. 168, 380–388.
Oremland, R.S., Stolz, J., 2000. Dissimilatory reduction of selenate and arsenate in nature. In: Environmental Microbe-Metal Interactions. Amer. Soc. Microbiology Press, Washington, D.C., pp. 199–224.
Oremland, R.S., Stolz, J.F., 2003. The ecology of arsenic. Science (New York, N.Y.) 300, 939–944.
Oremland, R.S., Stolz, J.F., Hollibaugh, J.T., 2004. The microbial arsenic cycle in mono Lake, California. FEMS Microbiol. Ecol. 48, 15–27.
Oremland, R.S., Saltikov, C.W., Wolfe-Simon, F., Stolz, J.F., 2009. Arsenic in the evolution of earth and extraterrestrial ecosystems. Geomicrobiol J. 26, 522–536.
Pace, A., Bourillot, R., Bouton, A., Vennin, E., Braissant, O., Dupraz, C., Duteil, T., Bundeleva, I., Patrier, P., Galaup, S., Yokoyama, Y., Franceschi, M., Virgone, A., Visscher, P.T., 2018. Formation of stromatolite lamina at the interface of oxygenic-anoxygenic photosynthesis. Geobiology 00, 1–21.
Páez-Espino, D., Tamames, J., de Lorenzo, V., Cánovas, D., 2009. Microbial responses to environmental arsenic. Biometals 22, 117–130.
Pivovarov, S., 2009. Diffuse sorption modeling. J. Colloid Interface Sci. 332, 54–59.
Rascovan, N., Maldonado, J., Vazquez, M.P., Eugenia Farías, M., 2016. Metagenomic study of red biofilms from diamante Lake reveals ancient arsenic bioenergetics in haloarchaea. ISME J. 10, 299–309.
Ravenscroft, P., Brammer, H., Richards, K., 2009. Arsenic Pollution: A Global Synthesis. John Wiley & Sons.
Renard, F., Putnis, C.V., Montes-Hernandez, G., Ruiz-Agudo, E., Hovelmann, J., Sarret, G., 2015. Interactions of arsenic with calcite surfaces revealed by in situ nanoscale imaging. Geochim. Cosmochim. Acta 159, 61–79.
Santini, J.M., Ward, S.A., 2012. The Metabolism of Arsenite. CRC Press.
Sforna, M.C., Philippot, P., Somogyi, A., Van Zuilen, M.A., Medjoubi, K., Schoepp-Cothenet, B., Nitschke, W., Visscher, P.T., 2014. Evidence for arsenic metabolism and cycling by microorganisms 2.7 billion years ago. Nat. Geosci. 7, 811–815.
Sforna, M.C., Daye, M., Philippot, P., Somogyi, A., Van Zuilen, M.A., Medjoubi, K., Gérard, E., Jamme, F., Dupraz, C., Braissant, O., Glunk, C., Visscher, P.T., 2017. Patterns of metal distribution in hypersaline microbialites during early diagenesis: implications for the fossil record. Geobiology 15, 259–279.
Smedley, P.L., Kinniburgh, D.G., 2002. Chapter 1 Source and Behaviour of Arsenic in Natural Waters. British Geological Survey, Wallingford, Oxon OX10 8BB, U.K.
Solé, V.A., Papillon, E., Cotte, M., Walter, P., Susini, J., 2007. A multiplatform code for the analysis of energy-dispersive X-ray fluorescence spectra. Spectrochim. Acta B At. Spectrosc. 62, 63–68.
Somogyi, A., Medjoubi, K., Baranton, G., Le Roux, V., Ribbens, M., Polack, F., Philippot, P., Samama, J.P., 2015. Optical design and multi-length-scale scanning spectro-microscopy possibilities at the nanoscopium beamline of synchrotron soleil. J. Synchrotron Radiat. 22, 1118–1129.
Sun, W., Sierra-Alvarez, R., Milner, L., Field, J.A., 2010. Anaerobic oxidation of arsenite linked to chlorate reduction. Appl. Environ. Microbiol. 76, 6804–6811.
Thiel, V., Tank, M., Neulinger, S.C., Gehrmann, L., Dorador, C., Imhoff, J.F., 2010. Unique communities of anoxygenic phototrophic bacteria in saline lakes of Salar de Atacama (Chile): evidence for a new phylogenetic lineage of phototrophic gammaproteobacteria from pufLM gene analyses. FEMS Microbiol. Ecol. 74, 510–522.
van Gemerden, H., 1993. Microbial mats: A joint venture. Mar. Geol. 113, 3–25.
Visscher, P.T., van den Ende, F.P., Schaub, B.E.M., van Gemerden, H., 1992. Competition between anoxygenic phototrophic bacteria and colorless sulfur bacteria in a microbial mat. FEMS Microbiol. Lett. 101, 51–58.
Witt-Eickschen, G., Palme, H., O'Neill, H.S.C., Allen, C.M., 2009. The geochemistry of the volatile trace elements As, Cd, Ga, In and Sn in the Earth's mantle: new evidence from in situ analyses of mantle xenoliths. Geochim. Cosmochim. Acta 73, 1755–1778.
Yamamura, S., Amachi, S., 2014. Microbiology of inorganic arsenic: from metabolism to bioremediation. J. Biosci. Bioeng. 118, 1–9.
Zhu, Y.-G., Yoshinaga, M., Zhao, F.-J., Rosen, B.P., 2014. Earth abides arsenic biotransformations. Annu. Rev. Earth Planet. Sci. 42, 443–467.
Zobrist, J., Dowdle, P.R., Davis, J.A., Oremland, R.S., 2000. Mobilization of arsenite by dissimilatory reduction of adsorbed arsenate. Environ. Sci. Technol. 34, 4747–4753.